Chemical Engineering Journal 546 (2026) 180111

Contents lists available at ScienceDirect

Chemical Engineering Journal

journal homepage: www.elsevier.com/locate/cej

Unravelling the kinetics of NH_3 decomposition over highly active Ru/CeO_2 catalysts: Effect of the support on H-poisoning and rate determining steps☆

Ivan Conti [a,1], Daniele Quattrin [b,1], Yi Qiu [a], Alessandro Trovarelli [b], Alessandra Beretta [a,*]

[a] Laboratory of Catalysis and Catalytic Processes, Dipartimento di Energia, Politecnico di Milano, via La Masa 34, 20156, Milano, Italy
[b] Dipartimento Politecnico di Ingegneria e Architettura, Università degli Studi di Udine, Via del Cotonificio 108, 33100, Udine, Italy

ARTICLE INFO

Keywords:
NH_3 decomposition
Ru/CeO_2
Kinetics
Mechanism
H-poisoning
Ru-hydrides

ABSTRACT

Ru/CeO_2 catalysts have recently gained attention for low temperature NH_3 decomposition: the combination of a highly active metal as Ru with a support as CeO_2, known to enhance several catalytic processes thanks to the ability to create oxygen vacancies, makes this formulation highly promising. In this study, the performances and kinetics of NH_3 decomposition over Ru/CeO_2 were investigated and compared with those of a reference Ru/Al_2O_3 catalyst by applying multiple techniques. Steady-state activity tests under diluted and concentrated conditions were performed to study the main kinetic dependences, develop rate laws and identify the nature of the rate determining steps. Dynamic experiments of adsorption/desorption and DRIFT experiments under flow conditions and with H_2/D_2 switch were conducted to identify and quantify the adsorbed species as well as the storage capacity and mobility of H-species, thus providing a support to the kinetic interpretation. The remarkable intrinsic activity exhibited by Ru/CeO_2 catalyst can be associated to the important mitigation of the H-poisoning effect that, instead, limits NH_3 decomposition over Ru/Al_2O_3. On Ru/CeO_2, intermediate H* species would easily migrate from the Ru-sites to the support, thereby hindering the formation of Ru-hydrides, which instead were visible on Ru/Al_2O_3. The higher catalytic activity of Ru/CeO_2 allowed a wider operating temperature range, which revealed that with decreasing temperature below 300 °C the rate-determining step of the reaction shifts from ammonia activation to N* associative desorption.

1. Introduction

Achieving global climate and energy targets requires large-scale deployment of renewable energy [1] and low-carbon energy carriers [2]. Hydrogen is increasingly recognized as a key enabler of the energy transition, connecting renewable electricity generation with hard-to-abate sectors such as heavy transport, shipping, aviation, and steel production [3]. Despite its potential, hydrogen storage and distribution remain major challenges due to its wide flammability range (4–75% in air), high diffusivity, and low volumetric energy density (9.8 kJ L^{-1}), which make compressed or cryogenic storage both costly and technically complex [4]. Chemical hydrogen storage offers a viable alternative, embedding hydrogen within stable molecules—so-called hydrogen carriers—that can be handled in liquid form under near-ambient conditions. Among these, ammonia stands out because of its high hydrogen content (17.8 wt%), ease of liquefaction (8.6 bar at 20 °C), and well-established production and transport infrastructure [5,6]. Current projections indicate that roughly 12 Mt. of H_2 per year will be traded as ammonia by 2030, though existing global infrastructure can accommodate only one-third of this amount. Therefore dedicated ammonia-cracking facilities are being developed across major European ports, with an expected combined capacity of approximately 1.5 Mt. H_2 yr^{-1} by 2030 [7].

$$2NH_{3\,(g)} \rightleftarrows N_{2(g)} + 3H_{2(g)} \quad \Delta H^0 = 46.22 \frac{kJ}{mol_{NH_3}} \tag{1}$$

Ammonia decomposition (Eq. (1)) is an endothermic reaction that proceeds with increase of the number of moles. This reaction is thus favoured at increasing temperature and decreasing concentration and pressure. Although thermodynamic equilibrium allows nearly complete NH_3 conversion at 400 °C and 1 atm, the reaction is strongly kinetically

☆ This article is part of a Special issue entitled: 'ICSET2025' published in Chemical Engineering Journal.

* Corresponding author.
E-mail address: alessandra.beretta@polimi.it (A. Beretta).

[1] These authors contributed equally to the work.

https://doi.org/10.1016/j.cej.2026.180111
Received 10 February 2026; Received in revised form 9 July 2026; Accepted 28 July 2026
Available online 31 July 2026

limited at these conditions. Consequently, the development of efficient catalysts and a fundamental understanding of their kinetic behaviour are crucial for designing compact and efficient ammonia crackers.

Regarding the reaction mechanism, NH_3 decomposition proceeds via stepwise dehydrogenation of NH_3 followed by the associative desorption of N_2 and H_2 [5], as reported in Eqs. (2)–(7):

$$NH_3 + * \rightleftarrows NH_3* \quad (2)$$

$$NH_3* + * \rightleftarrows NH_2* + H* \quad (3)$$

$$NH_2* + * \rightleftarrows NH* + H* \quad (4)$$

$$NH* + * \rightleftarrows N* + H* \quad (5)$$

$$N* + N* \rightleftarrows N_2 + 2* \quad (6)$$

$$H* + H* \rightleftarrows H_2 + 2* \quad (7)$$

N_2 dissociation is widely recognized as the rate-limiting step in ammonia synthesis [8]; however, in NH_3 decomposition, the dominant rate-determining step (RDS) is still a matter of debate. According to Ganley et al. [9], the RDS depends on the strength of the metal–nitrogen bond. Stronger M–N interactions would facilitate N—H cleavage but hinder N_2 desorption, whereas weaker M–N bonds would favour N_2 formation but limit NH_3 activation. Hence, an intermediate bond strength is expected to optimize catalytic activity. Their results suggest that nitrogen desorption limits the global process on Fe, Co, and Ni, whereas N—H bond scission limits the rate on Rh, Ir, Pd, Pt, and Cu. Tsai and Weinberg found that the RDS of NH_3 decomposition on Ru(0001) is temperature dependent: at lower temperatures, the reaction rate is determined by the recombinative desorption of nitrogen, while at temperatures above 750 K, the cleavage of the N—H bond in ammonia becomes the slowest step [10]. Bradford et al. proposed that both the NH_2—H bond cleavage and recombinative nitrogen desorption are rate determining steps over well dispersed Ru [11]. It was therefore suggested that the rate-determining step in ammonia decomposition varies with catalyst formulation and operating conditions [12].

Among the reported metals, Ru-based catalysts are recognized as the most active and stable for NH_3 decomposition [9]. Qiu et al. [13] performed a detailed kinetic study of NH_3 decomposition over Ru/$MgAl_2O_4$, Ru/MgO, and Ru/Al_2O_3 catalysts. All systems exhibited a strong inhibitory effect of adsorbed hydrogen, with the experimental data successfully fitted by a power-law model featuring a negative hydrogen reaction order. Despite this common behaviour, intrinsic activity varied with the support, that likely played a specific role in determining activity and kinetics by modulating metal dispersion, particle morphology, and electronic structure via metal–support interactions (MSI), as suggested by previous literature [14]. Building on this kinetic understanding, it is expected that the mitigation of the hydrogen poisoning by wakening the Ru-H* interaction and favouring the displacement of H* species from the catalytic site can a be very effective strategy to enhance the catalytic activity. Indeed, a dramatic boost of the reaction rate was demonstrated by Qiu et al. [15] by performing diagnostic O_2 co-feeding experiments where O_2 was used as efficient hydrogen scavenger. Such experiments now inspire the possibility to implement H-scavenging through the catalyst formulation, in such a way that the mobility of H* intermediates from the Ru site is enhanced and hydrogen inhibition is mitigated.

Ceria has recently emerged as an effective support for NH_3 decomposition. Ju et al. [16] reported the superior performance of Ru/CeO_2 relative to Ru/Al_2O_3 and Ru/SiO_2 and elucidated how Ru–CeO_2 interactions modify Ru electronic states, promoting electron back-donation that weakens the Ru—H bond. Yan et al. [17] confirmed this concept and proposed strategies to optimize Ru/CeO_2 interaction alleviating inhibitory desorption of H* upon Ru sites through direct desorption or spillover pathway. Furthermore, Hu et al. [18] proposed that ceria is able to influence ruthenium morphology favouring the formation of ~1.5 nm clusters, with enhanced activity in NH_3 activation [18].

Despite these advances, all revealing the potential of ceria as a support, quantitative kinetic descriptions of NH_3 decomposition over Ru/CeO_2 remain scarce, and mechanistic models that can effectively guide catalyst development are still lacking.

This work aims to address this gap through the development and validation of a mechanistically grounded kinetic model for NH_3 decomposition over Ru/CeO_2. The kinetic investigation was firstly performed by activity tests under diluted feed conditions to guarantee isothermal conditions and negligible heat and mass transfer limitations and the derived rate law was subsequently validated under concentrated feeds (up to 50% NH_3). A mechanistic foundation to the kinetic modelling was searched by additional experiments, including H_2-TPD and H_2/D_2 isotopic exchange experiments that were conducted to evaluate the hydrogen storage capacity and mobility, while NH_3-TPD and in situ DRIFTS were employed to characterize surface species involved in the reaction and to elucidate reaction intermediates. To better appreciate the effect of the nature of the support, the results of the study are herein discussed and systematically compared with those of a reference Ru/Al_2O_3 catalyst [13]. To enable a direct comparison, both catalysts were characterized and tested under identical conditions. Light was shed on the interpretation of the DRIFT experiments and of the nature of H-poisoning through the fundamental studies of Schoos and coworkers on Ru-hydrides [19,20].

2. Materials and methods

2.1. Catalyst preparation

Ru/Al_2O_3 and Ru/CeO_2 catalysts were synthesized by the incipient wetness impregnation (IWI) method using $Ru(NO)(NO_3)_3$ (Alfa Aesar, 1.5 wt% Ru mL^{-1}) as the metal precursor. Commercial γ-Al_2O_3 microspheres (Sasol Puralox SCCa) and commercial high-surface-area CeO_2 (kindly provided by Umicore) were employed as supports for the sake of generalization of the study. The CeO_2 support, supplied pre-calcined by the manufacturer (500 °C for 5 h), was used without further thermal treatment. In analogy, the γ-Al_2O_3 support was calcined prior to impregnation by heating from room temperature to 500 °C at 1 °C min^{-1} and holding 5 h. The precursor solution was prepared and added dropwise to the support under continuous mixing to achieve uniform pore filling. The impregnated material was then dried at 125 °C overnight. The nominal Ru loading was fixed at 1 wt%. The resulting catalysts are denoted in the following as Ru/Al_2O_3 and Ru/CeO_2. No post-impregnation calcination step was applied in order to preserve high metal dispersion, as calcination is known to promote particle growth and reduce dispersion on supported Ru catalysts [21].

2.2. Catalyst characterization and mechanistic DRIFTS experiments

Morphological properties were evaluated by N_2 adsorption–desorption at −196 °C using a Micromeritics TriStar 3000 instrument. Prior to analysis, the samples were degassed at 120 °C for 3 h.

X-ray diffraction (XRD) analysis was performed to characterize the catalyst structure using a Philips X'Pert diffractometer equipped with an X'Celerator detector and Ni-filtered Cu Kα radiation (λ = 1.542 Å, 40 kV, 40 mA). Data were collected on pre-reduced catalyst (reduction with temperature ramp under 5%H_2 flow from room temperature to 450 °C) in the 2θ range of 32–48° with a step size of 0.0167° and a scan rate of 0.00663° s^{-1}.

Metal particle dispersion was evaluated by CO pulse chemisorption, using a Micromeritics AutoChem II 2920 system equipped with a thermal conductivity detector (TCD) and the chemisorption procedure optimized by Felli et al. for ceria-containing catalysts [22]. The catalyst was loaded on a quartz wool bed in a U-shaped quartz reactor and

reduced under 5% H_2/N_2 (35 mL min^{-1}) with a temperature ramp of 5 °C min^{-1} from room temperature to 450 °C, followed by a 5 min He purge and cooling to 30 °C. The reduced catalyst was pretreated with 10% CO_2/He (35 mL min^{-1}) for 30 min, purged in He (35 mL min^{-1}) for 60 min, and subsequently exposed to successive 5% CO/He pulses (0.52 mL loop) until a steady-state response was reached.

Temperature-programmed reduction (TPR) was carried out using a Thermo Fisher TPD/R/O 1100 instrument to investigate the precursor decomposition and redox behaviour of the catalysts. A mass of 100 mg of fresh catalyst or support was loaded between quartz wool plugs in a quartz reactor and heated from room temperature to 450 °C under 4.89% H_2/Ar, followed by an isothermal hold of 1 h.

Thermogravimetric analysis (TGA) was performed with TA Instruments Discovery TGA 5500 to monitor catalyst and support weight loss with temperature. 15–20 mg catalyst was loaded on Pt sample holder and a temperature ramp of 10 °C min^{-1} was set under flowing 25 mL min^{-1} of N_2 or H_2.

Diffuse reflectance infrared Fourier transform spectroscopy (DRIFTS) was carried out to verify selective CO adsorption on Ru during chemisorption, to follow intermediates formed during NH_3 decomposition and to observe H—D exchange. A small amount of catalyst was loaded on a diffuseIR Pike cell, placed in a porous alumina crucible supported on a 100 μm quartz powder bed, and measurements were performed under a flowing gas stream of 50 mL min^{-1}. The catalysts were pretreated before every experiment at 450 °C under H_2 (5%)/N_2 for 55 min, purged for 5 min with He at 450 °C and cooled down under He flow before running experiments. The spectra were recorded on a Thermo Fisher Nicolet iS50 FTIR spectrometer equipped with a DTGS detector, using a resolution of 4 cm^{-1} over the 400–4000 cm^{-1} range. Two distinct procedures were used to investigate NH_3 decomposition intermediates and are described in the detail in the Supplementary Information: briefly, in the former, the reduced catalyst was exposed to 2.5% NH_3/He and the temperature was increased stepwise by 50 °C up to 400 °C, with 15 min holds at each step for spectra acquisition (Fig. S1); in the latter, the catalyst was contacted with NH_3 at room temperature, purged, and then heated in He following the same stepwise temperature program (Fig. S2).

For experiments of H—D exchange followed by DRIFTS, after the H_2 reducing pretreatment steps, a flow of 30 mL min^{-1} of D_2 (4%)/N_2 was set and the cell was saturated at room temperature. Then, temperature was raised to 400 °C with a ramp of 10 °C min^{-1} (Fig. S3) and spectra were acquired during this period. A different kind of H—D exchange experiments were also performed using a Micromeritics AutoChem II 2920 system equipped with a thermal conductivity detector (TCD) and connected to a OmniStar GSD 301 O mass spectrometer. Catalyst was loaded on a quartz wool bed in a U-shaped quartz reactor and reduced under 5% H_2/N_2 (35 mL min^{-1}) with a temperature ramp of 5 °C min^{-1} from room temperature to 450 °C, followed by 1 h of isotherm, 1 h He purge at 450 °C and cooling to −30 °C. Then the catalyst was exposed to D_2 (5%)/N_2, using a flow of 35 mL min^{-1}, and the system was heated up to 450 °C (Fig. S4). During this temperature ramp, mass signals 2, 3 and 4 were followed.

2.3. Steady state activity tests and temperature-programmed desorption experiments

Ru/CeO_2 catalysts were tested under both diluted and concentrated NH_3 streams using a micro–fixed-bed quartz reactor with an internal diameter of 9 mm, which was heated with electric tubular oven. The kinetic models were developed based on the diluted-feed experiments and subsequently validated under concentrated conditions, with NH_3 feed concentrations up to 50%. For reactor preparation, 300 mg of catalyst were diluted with quartz (1:1) of the same particle size resulting in a total bed height of 1 cm positioned between two quartz wool plugs. Quartz grain layer was placed before the catalyst bed to guarantee homogeneous distribution and heating of the feed. The particle size fraction was set to 75–106 μm for the kinetic tests, but additional tests were performed with larger particles (125–250 μm) to verify the absence of internal or external mass-transfer limitations. In the case of diluted NH_3 feeds, that is the conditions used for the kinetic model, a single point K-type thermocouple was positioned at the center of the catalytic bed; the negligible role of radial heat transfer limitations was controlled by the alignment of the inner temperature measurement with the external oven temperature and by application of the a-posteriori Mear's criteria [23] that were always largely satisfied, even in the conditions of high space velocity. In the case of tests with concentrated feeds, a TC-well with a movable thermocouple was inserted to monitor axial temperature gradients. The outlet gas composition was monitored by a ThermoStar quadrupole mass spectrometer (Pfeiffer Vacuum). The feed system comprised cylinders of pure NH_3, 2.55% NH_3/He, 5.03% H_2/Ar, pure H_2, N_2, and He for dilution.

Prior to each NH_3 decomposition experiment, the catalyst was pretreated in 1% H_2/He while heating from room temperature to 450 °C, followed by a 1 h hold. Activity tests were conducted between 200 and 500 °C at atmospheric pressure. The effect of NH_3 concentration was evaluated by varying the feed between 0.3%, 1%, and 2.55% NH_3 at a gas hourly space velocity (GHSV) of 20,000 $NL \cdot kg_{cat}^{-1} \cdot h^{-1}$ for kinetic model development, and at 10%, 30%, and 50% NH_3 for model validation. The influence of GHSV was studied in the 20,000–80,000 $NL \cdot kg_{cat}^{-1} \cdot h^{-1}$ range at a constant NH_3 concentration of 2.55%. Mixed experiments with H_2 co-feeding were carried out to quantify hydrogen inhibition and determine the reaction order: 0.3–1–2% NH_3 + 5% H_2, and 0.3–1% NH_3 + 25% H_2. In each experiment, material balance closure was verified through independent quantification of the molar flows of H_2, N_2, and NH_3, and by confirming that the N_2/NH_3, H_2/N_2, and H_2/NH_3 molar ratios approached the stoichiometric values.

Temperature-Programmed-Desorption (TPD) experiments were performed in the same reactor and testing rig. The total hydrogen storage capacity of the catalysts was evaluated by H_2-TPD adopting the following procedure illustrated in the Supplementary Information in Fig. S5 [24]: 1% hydrogen was adsorbed at 350 °C for 1 h and while cooling up to 50 °C, then switch to inert was performed, and after 1 h purge a temperature ramp from 50 °C to 450 °C with heating rate 5 °C min^{-1} was started, holding 1 h when 450 °C were reached. NH_3 temperature-programmed desorption (TPD) experiments were conducted on Ru/Al_2O_3 and Ru/CeO_2 catalysts to probe surface species formed at different adsorption temperatures. NH_3 pre-treatment (involving both adsorption and reaction) was carried out at several temperature levels, in between 150 and 350 °C for Ru/Al_2O_3 and in between 150 and 300 °C for Ru/CeO_2, with the procedure illustrated in Fig. S6. A gas mixture containing 1% NH_3 was fed to the reactor at the selected adsorption temperature for 1 h, followed by purging under inert gas flow for 1 h. The samples were then cooled to 150 °C and heated to 450 °C at a rate of 5 °C min^{-1}, with a dwell time of 1 h at the final temperature. Complementary 1% H_2 adsorption–desorption experiments were performed at 350 °C on Ru/Al_2O_3 and at 200 °C and 300 °C on Ru/CeO_2 following the same procedure.

2.4. Modelling methods

A 1-D pseudo-homogeneous plug flow reactor (PFR) model was adopted to describe the catalytic decomposition of ammonia under isothermal and isobaric conditions, assuming ideal plug flow and negligible mass transfer limitations. Species mass balances along the catalyst weight W were expressed as Eq. (8):

$$\frac{dF_i}{dW} = \nu_i \, r(T, P, \boldsymbol{y}) \, (1 - \gamma) \tag{8}$$

$$\gamma = K_p{}^{*}K_{eq}^{-1}(T) = \frac{P_{N_2}^{0.5} {}^{*} P_{H_2}^{1.5}}{P_{NH_3}} {}^{*} K_{eq}^{-1}(\mathrm{T}) \tag{9}$$

where F_i is the molar flow rate of species i, ν_i its stoichiometric

coefficient, r the intrinsic rate of the forward decomposition reaction, herein expressed as generic function of temperature T, pressure P and gas-phase composition $\boldsymbol{y}$. The thermodynamic consistency was accounted for by introducing the $(1-\gamma)$ term where γ, as described in Eq. (9), consists of in the ratio between the reaction quotient and the equilibrium constant in the rate expression, calculated with the correlations reported by Gillespie e Beattie [25].

The system of ordinary differential equations was solved numerically using MATLAB ode23s function, an adaptive solver suitable to stiff problems. The kinetic parameters were estimated through non-linear regression on experimental data using MATLAB lsqnonlin function, based on least-square method. The minimization objective was defined as the sum of squared errors between experimental and model-predicted conversions, normalized by experimental variance, which was estimated from repeated experiments conducted under a reference condition (1% NH_3) to verify catalyst stability and ensure data reproducibility. Model accuracy was assessed using the Mean Absolute Error (MAE) and Mean Absolute Percentage Error (MAPE%). The resulting kinetic model was then applied to design validation experiments, which were subsequently validated experimentally.

3. Results and discussion

3.1. Characterization

The morphological properties of the catalysts and the CO pulse chemisorption results are summarized in Table 1. The Ru/Al_2O_3 catalyst exhibits a higher specific surface area and pore volume compared to Ru/CeO_2, while the average pore diameters are nearly identical. In contrast, the CO uptake of the ceria-supported catalyst is approximately four times greater than that of Ru/Al_2O_3, indicating a substantially higher dispersion of Ru particles. Assuming a Ru:CO stoichiometric ratio of 0.6 [15], the calculated metal dispersions are 88% for Ru/CeO_2 and 21% for Ru/Al_2O_3.

To verify that CO adsorption occurred selectively on Ru surface sites rather than on the oxide supports, in situ DRIFTS measurements were performed. Upon CO_2 pre-treatment of the catalyst, carbonates-related bands were immediately observed. When CO was later introduced in pulses, these bands remained unchanged, indicating that CO adsorbed selectively on the ruthenium surface. The spectra and a more detailed discussion are provided in Fig. S7.

XRD patterns of the pre-reduced catalysts in the range of 2θ between 32 and 48 degrees are shown in Fig. 1. Reference patterns from the Powder Diffraction File (PDF) database were considered to identify crystalline phases. No diffraction peaks attributable to metallic Ru are detected (PDF: 00–001-1256), confirming the high dispersion of the active phase. The support-related reflections appear at 33.2° and 47.7° for CeO_2 (PDF: 01–075-0076), and at 37,44°, 39,67°, and 46,03° for γ-Al_2O_3 (PDF: 00-004-0875).

Temperature-programmed reduction (TPR) measurements under H_2 were performed for both supports and freshly prepared catalysts. The H_2 profiles from the TPR experiments is shown in Fig. 2 while the corresponding H_2 consumption is reported in Table 2.

Bare CeO_2 support showed the onset of H_2 consumption starting at 330 °C, consistent with surface ceria reduction: $Ce^{4+} \rightarrow Ce^{3+}$ [26]. On the contrary Al_2O_3 showed very weak H_2 consumption signal starting at

Table 1
Prepared catalysts characterization.

Name	BET surface area (m^2/g)	Pore volume (cm^3/g)	Pore diameter (Å)	CO/Ru
Ru/Al_2O_3	190	0.46	72	0.35
Ru/CeO_2	128	0.31	70	1.5

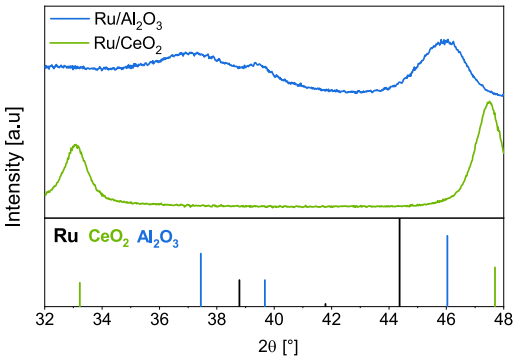

Fig. 1. XRD patterns of prepared catalysts.

150 °C, associated to minor reduction of surface impurities and hydroxyl groups desorption [27]. Upon Ru loading, both catalysts showed substantially higher H_2 consumption, associated with the precursor decomposition. Assuming complete reduction of all nitrate and nitrosyl ligands to N_2 and water with hydrogen, as described in Eq. (10), the maximum theoretical consumption associated with precursor decomposition can be estimated:

$$Ru(NO)(NO_3)_3 + 10H_2 \rightarrow Ru + 2N_2 + 10H_2O \quad (10)$$

Given 10 μmol of $Ru(NO)(NO_3)_3$ in the reactor before reduction, the stoichiometry predicts a maximum H_2 consumption of 100 μmol. If the H_2 consumed by the support during TPR is subtracted from the total consumed H_2 from the fresh catalyst, similar quantities are obtained for Ru/CeO_2 and Ru/Al_2O_3: 132 and 136 μmol respectively. Of those amounts, about 100 μmol are expected be consumed for the decomposition, and the excess are attributable to hydrogen chemisorbed on ruthenium. However, the two catalysts displayed distinctly different profiles: Ru/Al_2O_3 reduced broadly around 250 °C, whereas Ru/CeO_2 exhibited a sharp low-temperature peak near 150 °C with the highest uptake. This enhanced H_2 consumption, which exceeded that necessary for reduction of Ru precursor, indicates that part of the H_2 consumed in the low temperature region was involved in the removal of ceria surface oxygen through a spillover mechanism, reflecting the strong Ru–CeO_2 interaction.

Results of TG analyses on catalysts and supports up to 600 °C under H_2 and N_2 are reported in Fig. S8a and S8b: both supports exhibited only minor dehydration below 150 °C and remained stable at higher temperatures. Under H_2, the Ru-containing catalysts showed earlier and more pronounced weight losses than under N_2, confirming the promoting role of hydrogen in precursor decomposition and metal reduction. In reducing atmosphere, Ru/Al_2O_3 displayed a gradual mass decrease up to 300 °C, while Ru/CeO_2 decomposed in two distinct steps below 200 °C, indicating that CeO_2 facilitates precursor decomposition through strong metal–support interaction and high oxygen mobility. In contrast, under N_2, decomposition occurred more slowly and at higher temperatures, reflecting the formation of oxidized Ru species via incomplete nitrate breakdown. Overall, TGA and TPR analyses demonstrate that CeO_2 markedly improves the low-temperature reducibility of Ru species compared with Al_2O_3, leading to earlier activation, greater hydrogen consumption, and superior potential for catalytic applications requiring easily activated Ru sites.

3.2. H_2 storage capacity and mobility

Since hydrogen inhibition represents a major kinetic limitation of NH_3 decomposition over Ru-based catalysts, the interaction between hydrogen and the investigated materials was examined in detail.

Pieces of evidence on the storage capacity and mobility of H* species were searched by a series of complementary experiments. First, the interaction of hydrogen with Ru/CeO_2 and Ru/Al_2O_3 was studied

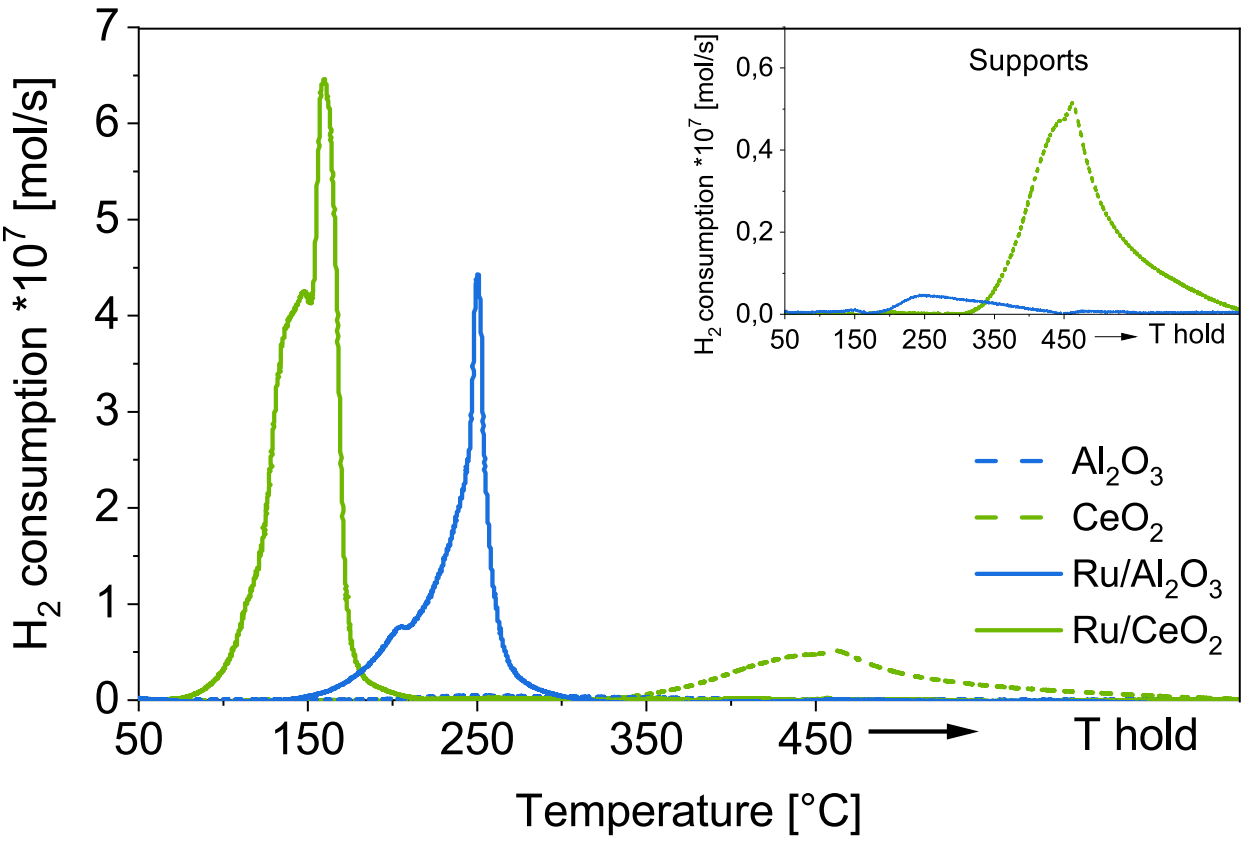

Fig. 2. H_2 TPR profiles of freshly-prepared catalysts and supports – 100 mg loaded in the reactor.

Table 2
Hydrogen consumption during H_2 TPR.

	CeO_2	Ru/CeO_2	Al_2O_3	Ru/Al_2O_3
Consumed H_2 [μmol]	90	222	9	145

through hydrogen adsorption/desorption experiments. Fig. 3 shows the desorbed hydrogen profiles after 1% H_2 adsorption from 350 °C to 50 °C, along with the relative quantification. Hydrogen desorption amounted to 46 μmol for Ru/CeO_2 and only 10 μmol for Ru/Al_2O_3; this large difference demonstrates that the ceria-supported catalyst has a substantially higher hydrogen storage capacity, being able to accommodate additional hydrogen on the surface of the support. In particular, the large amount of hydrogen desorption from Ru/CeO_2 occurred in a sustained way over a broad temperature range up to 450 °C, suggesting the presence of hydrogen species with different binding strengths [28], that

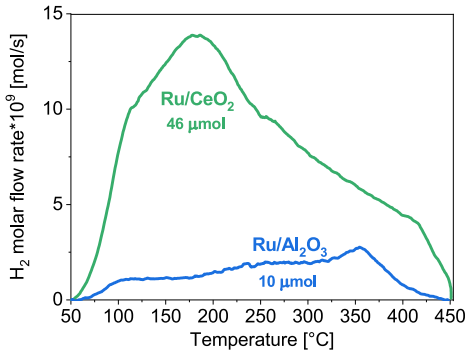

Fig. 3. H_2-TPD results after adsorption from 350 °C to 50 °C – 300 mg catalyst loaded in the reactor.

could be associated with both Ru nanoparticles and the support through spillover phenomena.

To better elucidate the role of the support, through spillover of H-species from the Ru particles, isotopic exchange with deuterium, followed by DRIFTS spectroscopy, was carried out. The catalyst was subjected to a reducing pretreatment by heating from room temperature to 450 °C under H_2 (5%)/N_2 for 1 h, then cooled under N_2 to room temperature and subsequently heated to 400 °C under a flow of D_2 (4%)/N_2. DRIFTS spectra were recorded during this treatment and are shown in Fig. 4. On Ru/Al_2O_3 at room temperature the band of O—H stretching is clearly visible between 2500 cm^{-1} and 4000 cm^{-1}. Similar observations are possible for Ru/CeO_2: O—H band is recognized between 2500 cm^{-1} and 4000 cm^{-1}, residual carbonates give rise to the peaks around 1500 cm^{-1} and Ce—O vibrations and bendings are visible below 1200 cm^{-1} [29,30]. In both cases, isotopic exchange started to take place as soon as temperature increased to 40 °C, since the intensity of the O—H stretching band decreased while O—D stretching bands, between 2800 cm^{-1} and 1800 cm^{-1}, rose.

The spectra in Fig. 4 show that whereas on Ru/CeO_2 the H—D switch was almost complete at 40 °C, on Ru/Al_2O_3 the O—H band was still present at 40 °C and progressively decreased with increasing temperature. The difference between the two catalysts is thus related to the different speed of H—D substitution. Indeed, on Ru/CeO_2 the O—H band suddenly disappeared at 40 °C, while on Ru/Al_2O_3, the process started at 40 °C where the O—H band was only partially substituted by the O—D band. As temperature increased, on the cerium dioxide sample no substantial modifications of the spectra took place, whereas on the alumina sample the H—D exchange proceeded and was not fully complete even at 400 °C. When considering also the much larger H-storage capacity of Ru/CeO_2 with respect to Ru/Al_2O_3 revealed by the TPR experiments, the difference response to H—D switch tests suggests very different Ru-H* strength and hydrogen/deuterium mobility on the support. It can be assumed that on alumina the metal activated D_2 and probably catalysed

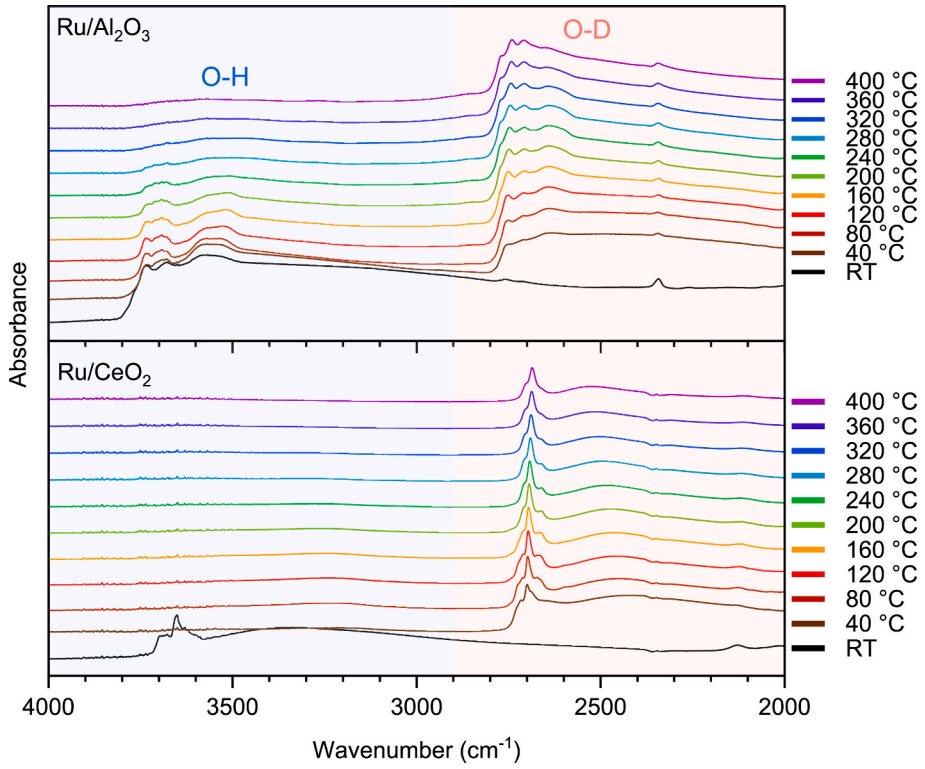

Fig. 4. In situ DRIFTS spectra during D_2 TPR on pre-reduced catalyst.

the isotopic exchange on the nearby portion of surface, while on cerium dioxide both the activation of D_2 molecules and the migration of deuterium atoms to the support have been faster, rapidly substituting nearly all the O—H groups on the oxide surface.

The H—D substitution behaviour of Ru/CeO_2 and Ru/Al_2O_3 was also monitored by mass spectrometry during D_2 temperature-programmed reaction (TPR) experiments initiated at −30 °C on catalysts pre-reduced in H_2. The resulting profiles, shown in Fig. 5, confirmed the trends previously observed by in situ DRIFTS. In the case of Ru/Al_2O_3, a broad deuterium consumption was observed over the temperature range 25–250 °C, accompanied by the formation of a broad HD desorption peak within the same interval. In contrast, in the case of Ru/CeO_2, deuterium consumption and the subsequent HD production were confined to a much narrower temperature window (10–100 °C),

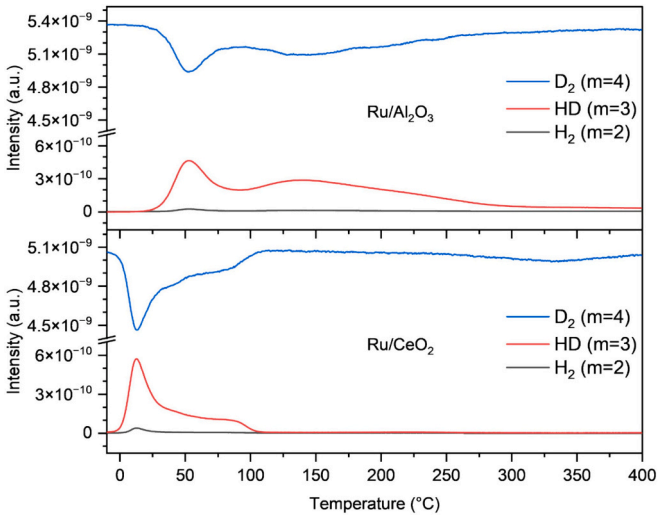

Fig. 5. Mass spectrometer signals during D_2 TPR.

confirming that the ceria-based catalyst promotes isotopic exchange by displacing hydrogen with significantly faster kinetics.

Globally, it can be concluded that on the Ru/CeO_2 catalyst much larger mobility of the H* species was driven by favourable kinetics and larger storage capacity, and that both factors are reasonably associated to the strong metal-support interaction and the peculiar functionality of the support, especially ceria reducibility.

3.3. Kinetic investigation

The Ru/Al_2O_3 catalyst was previously investigated under diluted conditions (up to 2.55% NH_3) by Qiu et al. [13], who performed experiments at varying NH_3 concentrations and under product co-feeding. The study reported an apparent self-inhibition by NH_3, reflected in a reaction order between 0 and 1, and a strong inhibitory effect of hydrogen, with a kinetic order of −1.5. N_2 co-feeding had no measurable influence on NH_3 conversion. A simple power-law model (Eqs. (11) and (12)) was proposed to describe the experimental data, especially those representative of large H_2 concentrations as expected under real applicative conditions:

$$r = k(T)\frac{P_{NH_3}}{P_{H_2}^{1.5}} \qquad \left[\frac{mol_{NH_3}}{s\, g_{cat}}\right] \tag{11}$$

$$k(T) = 2.81E-8{*}\exp\left(-\frac{45600}{1.987}{*}\left(\frac{1}{T}-\frac{1}{600}\right)\right) \left[\frac{mol_{NH_3}{*}atm^{0.5}}{s\, g_{cat}}\right] \tag{12}$$

This rate expression was derived under the assumption that the rate-determining step of NH_3 decomposition lies within the NH_3 activation pathway, specifically the second dehydrogenation step, with the surface nearly saturated by adsorbed hydrogen although it was recognized that a reaction order on NH_3 lower than 1 was more representative of the NH_3 adsorption phenomena under conditions characterized by NH_3-rich and H_2-lean conditions (e.g. low temperature and low conversion), as recalled in Fig. S9.

The kinetic study of Ru/CeO_2 followed the same protocol as Ru/

Al_2O_3 and was subsequently extended to include a wider range of kinetically relevant conditions. The results obtained under 0.3–1.0–2.55% NH_3, as well as under 5–10–25% H_2 co-feeding (at a fixed 1% NH_3), are shown in Fig. 6a. Increasing NH_3 concentration produced a clear shift of the conversion curves toward higher temperatures, indicating an apparent fractional reaction order with respect to NH_3. At 300 °C, NH_3 conversion decreased from 98% to 52% as NH_3 concentration increased from 0.3% to 2.55%. To verify the presence and intensity of H_2-poisoning, co-feeding experiments were also performed: at 320 °C, NH_3 conversion dropped from 95% to 4% when 25% H_2 was added, confirming a pronounced hydrogen inhibition effect. Also the effect of contact time was investigated by varying the GHSV between 20,000 and 80,000 $Ncc \cdot h^{-1} \cdot g_{cat}^{-1}$ at constant 2.55% NH_3. As shown in Fig. 6b, NH_3 conversion increased with both contact time and temperature, reflecting enhanced reaction rates within the kinetic regime.

A comparison between Ru/CeO_2 and Ru/Al_2O_3 activities under reference operating conditions is presented in Fig. 7. The ceria-supported catalyst exhibits significantly higher activity. Under 1% NH_3 at 300 °C, conversion increased from 15% (Ru/Al_2O_3) to 80% (Ru/CeO_2), and under 25% H_2 at 440 °C, from 29% to 96%. Moreover, the shift of the 1% NH_3 conversion curve induced by 25% H_2 co-feeding was less pronounced for Ru/CeO_2 (≈95 °C at about 60% conversion) than for Ru/Al_2O_3 (≈114 °C at about 60% NH_3 conversion), indicating partial mitigation of hydrogen poisoning by the ceria support despite the measured large H_2-storage capacity—a phenomenon explored in detail in Section 3.2.

Simple power-law models failed to describe the behaviour of Ru/CeO_2 in the entire operating field, which displayed more complex kinetic dependences. Assuming pseudo–first-order conditions, apparent rate constants were extracted from the experimental data and used to construct an Arrhenius plot (Fig. 8a). Two major observations can be drawn from the results, concerning the temperature dependence and the concentration dependence. A clear change of the apparent activation energy between low- and high-temperature regimes was observed (approximately across 300 °C). The onset of mass-transfer limitations was excluded by evaluating the Weisz–Prater modulus [31], which yielded a value of 0.007 ≪ 1, and also by performing additional experiments using larger catalyst particle sizes. As shown in Fig. S11, these tests resulted in comparable conversions, confirming the absence of internal diffusion limitations. The change of slope shown in Fig. 8a can thus be associated to a change of the rate determining step. Besides, a global kinetic order below unity is revealed both at low and higher temperatures. To further elucidate the impact of ammonia concentration and the resulting reaction order, the data were also analysed under pseudo–zero-order assumption (Fig. 8b). This analysis confirmed the change of the apparent activation energy but better highlighted also a change of kinetic orders, which further supports the hypothesis of a

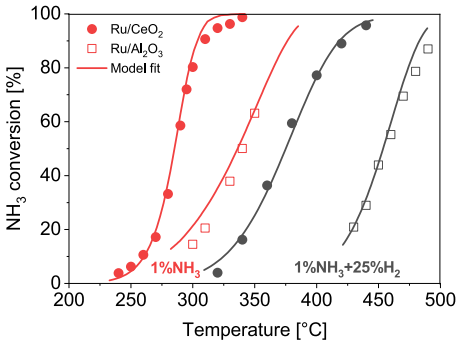

Fig. 7. Activity comparison between Ru/CeO_2 and Ru/Al_2O_3 catalysts in reference conditions: 1% NH_3 and 1%NH_3 + 25%H_2.

change in the nature of the rate-determining step; in particular, under the diluted conditions herein adopted, the measured effect of NH_3 on conversion in the low temperature range reduced to a zero-order kinetic dependence. In the literature, the temperature-dependent change in the rate-determining step of NH_3 decomposition was first reported by Tsai and Weinberg [10], who demonstrated that the rate-determining step on Ru(0001) varies with temperature. At lower temperatures, the reaction rate was proposed to be controlled by the recombinative desorption of nitrogen, whereas at higher temperatures, cleavage of the N—H bond in ammonia was proposed to become the slowest step. More recent DFT studies [12] have confirmed that N—H bond scission and nitrogen recombination are the two most critical elementary steps in ammonia decomposition, while also showing that the associated energy barriers depend strongly on Ru particle size, metal–support interactions, and operating conditions.

Based on the evidence provided by data in Fig. 8b and the literature reports, we herein assume that in the low temperature window N_2 desorption ($2\,N^* \rightarrow N_2 + 2^*$) is the rate-determining step (RDS) and that N^* is the most abundant surface intermediate (MASI), global zero-order kinetic model with respect to ammonia was obtained, as reported in Eq. (13):

$$r_{N_2} = k_{N_2}(T)\frac{P_{NH_3}^2 \Big/ P_{H_2}^3}{\left(1 + K\,P_{NH_3} \Big/ P_{H_2}^{\frac{3}{2}}\right)^2} = k_{N_2}(T)\frac{P_{NH_3}^2}{\left(P_{H_2}^{\frac{3}{2}} + K\,P_{NH_3}\right)^2} \tag{13}$$

Here, K represents the lumped equilibrium constant for the formation of N^* from NH_3. It can be expressed as the product of the equilibrium constants associated with NH_3 adsorption, the stepwise dehydrogenation reactions (Eqs. (3)–(5)), and hydrogen desorption, as shown in Eq. (14).

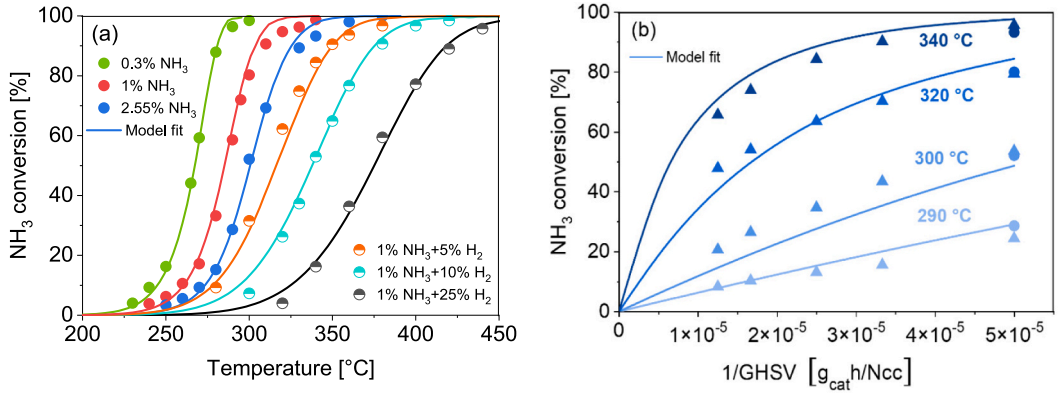

Fig. 6. Experimental and modelling results for NH_3 decomposition over a Ru/CeO_2 catalyst under varying NH_3 concentrations and H_2 co-feeding conditions (a), and at different GHSV (b). In panel (b), triangular and dotted symbols denote repeated experiments, illustrating the experimental uncertainty.

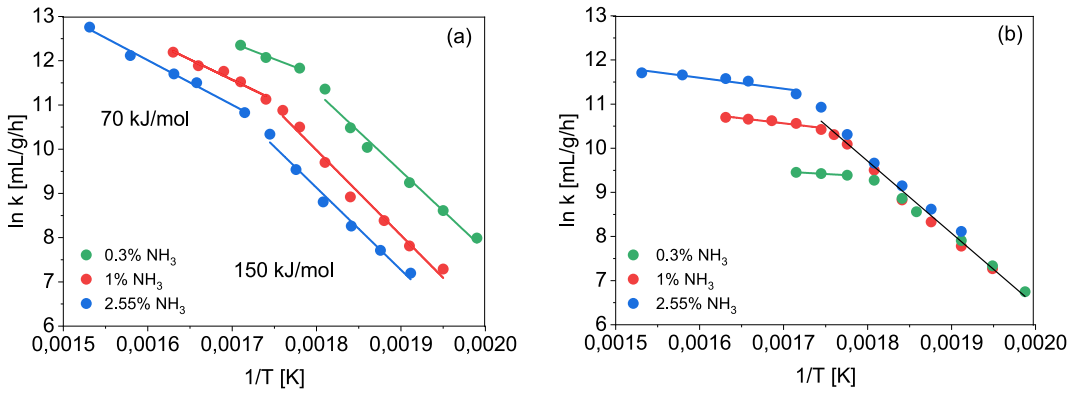

Fig. 8. Pseudo first-order (a) and pseudo zero-order (b) analysis of measured NH_3 conversion data on Ru/CeO_2 at varying NH_3 concentration - GHSV = 20,000 Nl/h/kg_{cat}.

$$K = K_{ads}^{NH_3} * K_{dehyd_1} * K_{dehyd_2} * K_{dehyd_3} * K_{H_2}^{-\frac{3}{2}} \quad (14)$$

The detailed derivation of the rate expression and of the lumped equilibrium constant K, including the formulation of the site balance and elimination of intermediate species, is provided in the Supplementary Information (Section S4.1).

At higher temperatures, instead, the data reported in Fig. 8a,b reveal a global kinetic order on ammonia between zero and one, in analogy with the typical kinetic dependences that the reaction show over Ru/Al_2O_3 and other Ru-supported catalysts in the same temperature range [13]. By assuming, in analogy with the kinetic analysis of the Ru/Al_2O_3 data, that also on Ru/CeO_2 NH_3 activation, namely the second NH_3 dehydrogenation, becomes the limiting step ($NH_2^* + * \rightarrow NH^* + H^*$) with H* as MASI, the kinetic model in Eq. (15) was derived:

$$r_{NH_2-H} = k_{NH_2-H}(T) \frac{P_{NH_3}}{P_{H_2}^{0.5}\left(1 + (K_{H_2}P_{H_2})^{0.5}\right)^2} \quad (15)$$

The complete derivation of this expression, including the treatment of quasi-equilibrated steps and the application of the site balance under H* as MASI, is provided in the Supplementary Information (Section S4.2).

Despite the formal linear dependence on NH_3, such reaction rate, at high NH_3 conversion and appreciable H_2 surface coverage, reproduce a global kinetic order below unity, in line with the experimental evidence.

In order to describe the entire temperature and compositional operating window with a single rate expression, the two limiting kinetic regimes in Eqs.(13) and (15) were combined. A simple mathematical strategy of interpolation of limiting trends was adopted:

$$\frac{1}{r} = \frac{1}{r_{N_2}} + \frac{1}{r_{NH_2-H}} \quad (16)$$

This approach corresponds to a two capacitance-in-series model and ensures in a simple mathematical form that the slowest step dominates the overall rate both in the limiting regimes, and in the transition between the two, as shown by the profiles reported in Fig. S11 in the Supplementary Information.

For the sake of completeness, the correction term to account for the thermodynamic consistency is also reported in the following:

$$r_{NH_3} = \left(\frac{1}{k_{N_2}(T)\frac{P_{NH_3}^2}{\left(P_{H_2}^{\frac{3}{2}} + K\, P_{NH_3}\right)^2}} + \frac{1}{k_{NH_2-H}(T)\frac{P_{NH_3}}{P_{H_2}^{0.5}\left(1+(K_{H_2}P_{H_2})^{0.5}\right)^2}} \right)^{-1} (1-\gamma) \quad (17)$$

$$k_{N_2}(T) = k_{N_2}(580K)\exp\left(-\frac{E_{act,\ N_2}}{R}\left(\frac{1}{T} - \frac{1}{580}\right)\right) \quad (18)$$

$$k_{NH_2-H}(T) = k_{NH_2-H}(640K)\exp\left(-\frac{E_{act,NH_2-H}}{R}\left(\frac{1}{T} - \frac{1}{640}\right)\right) \quad (19)$$

The complete model was adapted to the bulk of experimental data collected at varying temperature, GHSV and feed composition; the result of the model fit is shown in Fig. 6a,b.

The estimated kinetic parameters are listed in Table 3, where 95% confidence intervals are also reported. The confidence intervals were calculated assuming an experimental variance of $2*10^{-3}$, estimated from repeated experiments of NH_3 decomposition under 1% and 2.55% NH_3 conditions. The correlation matrix is provided in the Supplementary Information (Table S1). Overall, the absence of significant correlations indicates that the parameters are independent and the model robust.

In practice, N_2 desorption governs the overall rate at low temperatures, whereas dehydrogenation becomes rate-determining at high temperatures.

The model fit to the bulk of data is largely satisfactory, when considering the limited number of adaptive parameters introduced, as shown by the solid lines in Fig. 6a,b; the description of the experimental data set shows in fact a good agreement, yielding a mean absolute error (MAE) of 2.8% and a mean absolute percentage error (MAPE) of 12.5%, both within the experimental uncertainty.

Additional repeated experiments were performed under these conditions (Fig. 6b) to assess reproducibility, confirming that the observed deviations are consistent with the experimental variability. Overall, the model accurately and robustly captures the kinetic trends across the investigated conditions.

Minor deviations are observed in Fig. 6b at 300 °C, a critical operating condition, intermediate between the limiting kinetic behaviours. Such deviations are believed acceptable, when considering the simple mathematical architecture of the kinetic model where the interpolation of limiting kinetic trends is described without introduction of weighing functions or additional adaptive parameters.

Table 3
Estimated kinetic parameters for Ru/CeO_2 catalysts.

Low T kinetics – N_2 desorption is RDS			High T kinetics – NH_2-H is RDS		
$k_{N_2}(580K)$	E_{act,N_2}	K	$k_{NH_2-H}(640K)$	$E_{act,\ NH_2-H}$	K_{H2}
$\frac{mol_{NH_3}*atm}{s*g_{cat}}$	$\frac{kcal}{mol}$	$atm^{0.5}$	$\frac{mol_{NH_3}}{s*g_{cat}*atm^{0.5}}$	$\frac{kcal}{mol}$	atm^{-1}
(6.8 ± 1.1) E-5	42.2 ± 2.4	3.4 ± 0.3	(8.1 ± 1.3) E-3	25.8 ± 2.1	310 ± 40

In order to stringently verify the kinetic conclusions, the model was employed in simulation mode to design experiments that might provide an unambiguous verification of the embedded kinetic dependences. In particular, considering that the low temperature kinetics (Eq. 5) yields a rather unique dependence on NH_3 with order potentially variable in between zero and two, experimental conditions were searched where such kinetic dependence could emerge and affect significantly the reactor response. Indeed, it was easily recognized that, in the presence of large hydrogen concentrations, the rate expression of N_2 desorption is expected to reduce to a pure second order dependence on NH_3, as illustrated in Eq. (20):

$$r_{N_2} = k_{N_2}(T)\frac{P_{NH_3}^2}{\left(P_{H_2}^{\frac{3}{2}} \gg K^* P_{NH_3}\right)^2} \sim k_{N_2}(T)P_{NH_3}^2 \Big/ \text{constant} \tag{20}$$

Simulations were thus obtained at varying NH_3 concentrations, by assuming H_2 co-feeding at 5% and 25%, representative of moderate and large H_2 content; the modelling results are shown in Fig. 9. They indicate that under low H_2 partial pressures, the predicted overall kinetic order in NH_3 is below unity, thus an increase of NH_3 concentration is expected to produce a decrease of conversion, whereas in hydrogen-rich conditions, the predicted NH_3 dependence grows beyond the linearity such that at increasing NH_3 concentration the conversion is expected to grow. Once identified the conditions that could reveal the kinetic relevance of the low the temperature rate determining step, experiments were performed; the results are reported in Fig. 9 in symbols and fully confirm the model predictions, showing a negative effect of NH_3 concentration at low H_2 content and a positive effect of NH_3 at high H_2 content. We believe that is a very powerful validation of the kinetic assumptions that support the model derivation.

Finally, to verify the robustness of the proposed kinetic model, experiments with 10–30-50%NH_3/Ar were performed, which results are reported in symbols in Fig. 10. At high conversion levels (30% and 50% NH_3), rigorous isothermal behaviour could not be guaranteed; as documented in detail in the Supplementary Information (Fig. S11), radial temperature gradients presumably developed between the oven setpoint and the catalyst bed axial position, with a maximum deviation of 26 °C under the most severe conditions (highest concentration and conversion), due to the strongly endothermic nature of the reaction. Instead, axial temperature gradients were of minor extent. For this reason, temperature error bars have been added in Fig. 10. The model predictions were in fact obtained under the assumption of isothermal behaviour at the average bed temperature measured by the axial

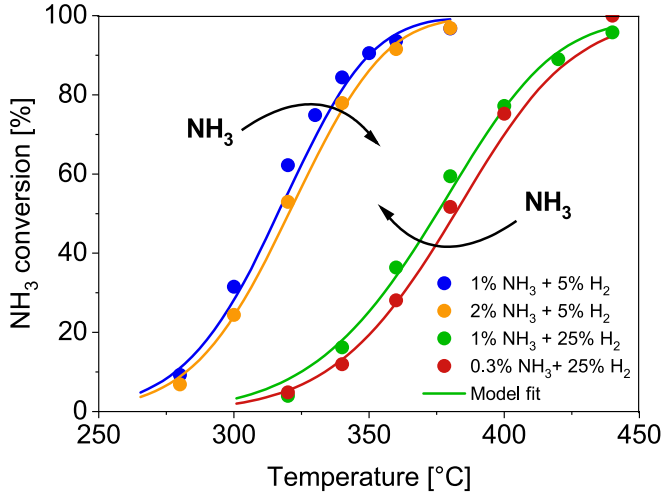

Fig. 9. Prediction of variable apparent kinetic order on NH_3 for Ru/CeO_2, depending on H_2 content. Lines = model predictions; symbols = validation experiments. (GHSV = 20,000 NL/h/Kg_{cat}).

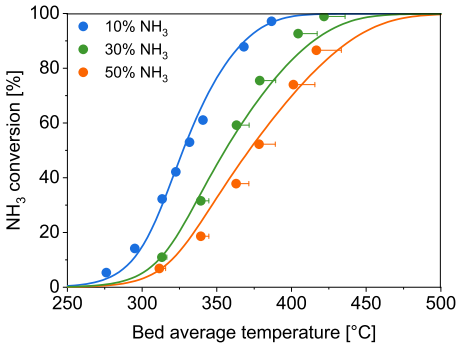

Fig. 10. Validation experiments for Ru/CeO_2 kinetic model – concentrated NH_3 feeds (GHSV = 20,000 Nl/h/Kg_{cat}).

thermocouple; the bars estimate the possible maximum temperature uncertainty due to the difference between inner and oven temperature measurements. Despite such uncertainty, the model predictions closely match the observations, reproducing in a faithful way the important decline of conversion at increasing NH_3 concentration and thus demonstrating robust predictive capability.

3.4. *Surface species investigation: TPD after NH_3 and H_2 pretreatments*

Independent pieces of evidence on the nature of surface species that characterize the investigated Ru-catalysts at varying temperatures were searched by developing a methodology of sequential reaction and desorption steps. In particular, in each experiment the catalyst was exposed to reacting conditions (at a given temperature and NH_3 feed concentration), then extensively purged in He in order to preserve only the more strongly bound species, that were finally desorbed in flowing inert gas under temperature ramp. As a consequence of the extensive purge following the adsorption phase, a conservative estimation of the adsorbed surface species is expected from the experiments.

For the Ru/Al_2O_3 catalyst, the concentration profiles of the desorbing species after pre-treatment in 1% NH_3 at 150, 300, and 350 °C are shown in Fig. 11.

The pre-treatment at 150 °C (a temperature well below the onset of measurable conversions) was followed by the release of NH_3, N_2 and H_2 during the desorption phase (Fig. 11a). The overall quantity of the desorbing species is comparable with the 30 Ru μmol in the reactor, indicating extensive surface coverage, in line with the reaction hindrance at this temperature. The N_2 desorption profile displayed two distinct features: a low-temperature peak assigned to the recombinative desorption of surface N* species, and a second peak that was simultaneous with H_2 evolution and in a 3:1 H_2:N_2 stoichiometric ratio, thus characteristic of NH_3 decomposition. These observations suggest the coexistence of NH_3* and N* surface intermediates on the catalyst surface. Increasing the pretreatment temperature at 300 °C markedly reduced the amount of desorbing species (Fig. 11b), indicating a cleaner surface that allowed the reaction to proceed. Under these conditions, only simultaneous H_2 and N_2 desorption signals were observed, with an H_2/N_2 ratio approaching the stoichiometric value of 3, as shown in Fig. 11b. NH_3* is thus the expected main adsorbed species at this temperature, close to the onset of the reaction. Finally, at further increasing pre-treatment temperature at 350 °C the desorbed quantities markedly declined, indicating a cleaner surface, consistently with the ≈ 60% NH_3 conversion observed at this temperature. A single N_2 desorption peak was observed, overlapping with H_2 evolution; the hydrogen signal greatly exceeded the stoichiometric amount of decomposition, suggesting the presence of surface H* species together with some NH_3* species. Notably, the H_2 desorption signal after NH_3 pretreatment was significantly higher than the one obtained from a H_2-TPD experiment that was performed with the same adsorption-purge-desorption

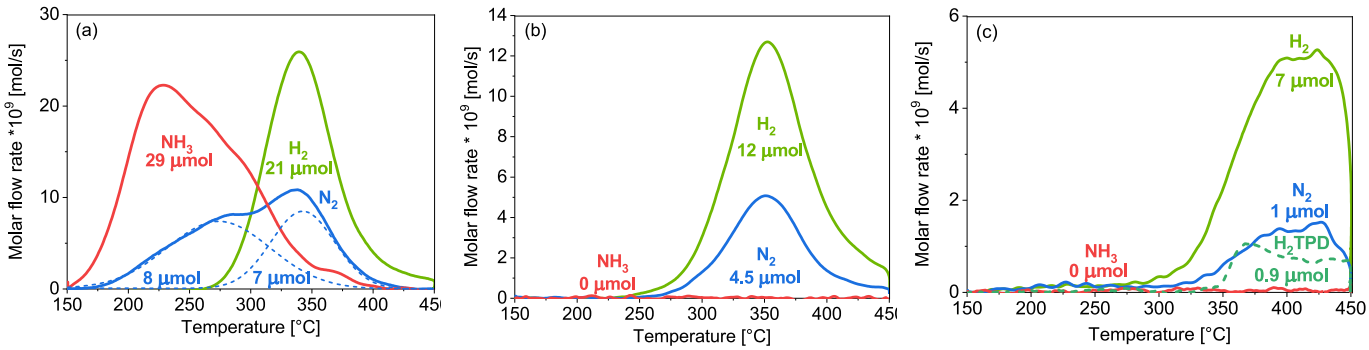

Fig. 11. Ru/Al_2O_3 1% NH_3-TPD spectra after adsorption at 150 °C (a) 300 °C (b) and 350 °C (c).

procedure as the reactive experiments (and reported in Fig. 11c as dotted line). This suggests that the surface coverage of H* species was essentially due to the N—H bond cleavage on Ru sites, rather than adsorption from molecular H_2.

The entire data set of reaction–desorption experiments performed at several intermediate temperatures is reported in detail in the Supplementary Information; Figs. S12 reveal a smooth transition between the single cases extracted and reported in Fig. 11. The same methodology of quantification of surface species was applied at each temperature. In particular, the amount of decomposed surface NH_3 was estimated from the gas phase products H_2 and N_2 accounting for the stoichiometric 3:1 ratio (and taking as pivot the less abundant of the two species), while total adsorbed NH_3* was calculated as the sum of the decomposed NH_3* and the molecularly desorbed NH_3. The coverage of H* and N* were estimated based on the quantities of detected H_2 and N_2, not explained by NH_3* decomposition. The global trends are reported in Fig. 12. N* and NH_3* result largely abundant surface species in those low temperature conditions where no conversion could be observed, whereas at increasing temperatures above 300 °C, N* coverage was negligible, NH_3* coverage declined importantly and H* coverage increased and became the most abundant surface intermediate; which is in line with the expected kinetic regime characterized by the limiting role of NH_3 activation and the poisoning from H* species.

In particular the desorption profiles are consistent with the simple power-law kinetic model previously proposed [13], but also suggest that future refinements could incorporate explicit ammonia adsorption terms in the lower temperature regime to enhance its predictive accuracy.

The same experiments were performed with the Ru/CeO_2 catalysts and Fig. 13 reports the results obtained at 150, 200, 300 °C, respectively.

Pretreatment at 150 °C (Fig. 13a) resulted in a small NH_3 desorption signal, together with two non-simultaneous N_2 and H_2 desorption peaks. N_2 desorption completed at about 350 °C, whereas H_2 was released over the entire temperature range up to 450 °C. The N_2 desorption peak is consistent with the recombinative desorption of adsorbed N* species on Ru sites, while the associated H_2 desorption might possibly arise from both hydrogen adsorbed on Ru and hydrogen released from the support. However, the broad and slow H_2 desorption profile indicates a significant contribution from hydrogen storage capacity of the support. Compared to Ru/Al_2O_3 (Fig. 11a), the significantly lower amounts of desorbed species at 150 °C indicate a cleaner surface on Ru/CeO_2, which is consistent with its intrinsically higher NH_3 decomposition activity. Upon increasing the pretreatment temperature to 200 °C (Fig. 13b), NH_3 desorption was no longer observed; also the intensity of N_2 desorption peak significantly declined from 4 to 2.5 µmol, as expected from a surface coverage on Ru sites. In contrast, H_2 desorption increased markedly to 19.5 µmol and exhibited a broadened profile. Notably, the hydrogen desorption trace closely matches the one obtained from a H_2-TPD experiment that was performed with the same adsorption-purge-desorption procedure as the reactive experiments (and reported in Fig. 13b as dotted line), indicating that the release profile after exposure to NH_3 is mainly representative of the catalyst H-storage capacity, rather than the hydrogen formation/desorption kinetics. These results closely align with those of the experiments performed to investigate H-adsorption and mobility and can be explained by the role of ceria as an effective hydrogen reservoir. Furthermore, at the pretreatment temperature of 300 °C (Fig. 13c), no NH_3 desorption was detected, confirming high activity and complete NH_3 conversion during the pretreatment. H_2 signal dominated the desorption phase, reaching 10.63 µmol and closely matching the H_2-TPD reference (9.8 µmol), while only a minor N_2 desorption signal was observed. This behaviour confirms extensive hydrogen storage on ceria and a strongly reduced surface coverage of nitrogen species on Ru.

Overall, these results demonstrate that N* species, present on the surface at low temperatures where the onset of catalyst activity lies, progressively diminished with increasing temperature due to recombination and desorption kinetics, while ceria increasingly acted as a hydrogen storage medium through spillover, presumably guaranteeing H-scavenging from Ru sites and higher activity. This picture aligns very well with the kinetic understanding of the reaction on Ru/CeO_2, derived from the activity tests, according to which a general higher activity with respect to the reference Ru/Al_2O_3 can be associated to a cleaner surface with displacement of H* from the metal sites to the support, with a characteristic abundance of N* species in low temperature regime.

An additional NH_3-TPD experiments was performed at 250 °C, and the results aligned with the general temperature effect are reported in Fig. S13. Similarly to the case of Ru/Al_2O_3, the general evolution of the surface-adsorbed species on Ru/CeO_2 is presented in Fig. 14. Adsorbed hydrogen remains the dominant species throughout the temperature window. The amount of adsorbed nitrogen sharply decreased with temperature, particularly within the catalyst's activity range. The desorbing NH_3 was almost negligible on Ru/CeO_2 with respect of Ru/Al_2O_3.

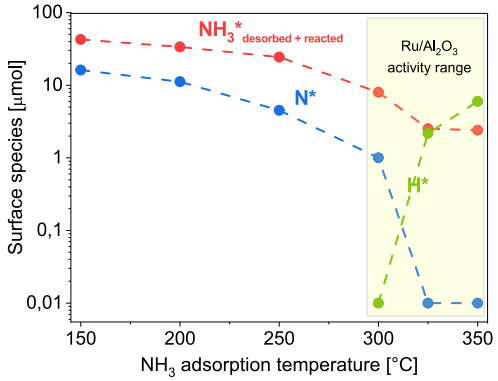

Fig. 12. Estimated surface species after 1% NH_3 adsorption over Ru/Al_2O_3.

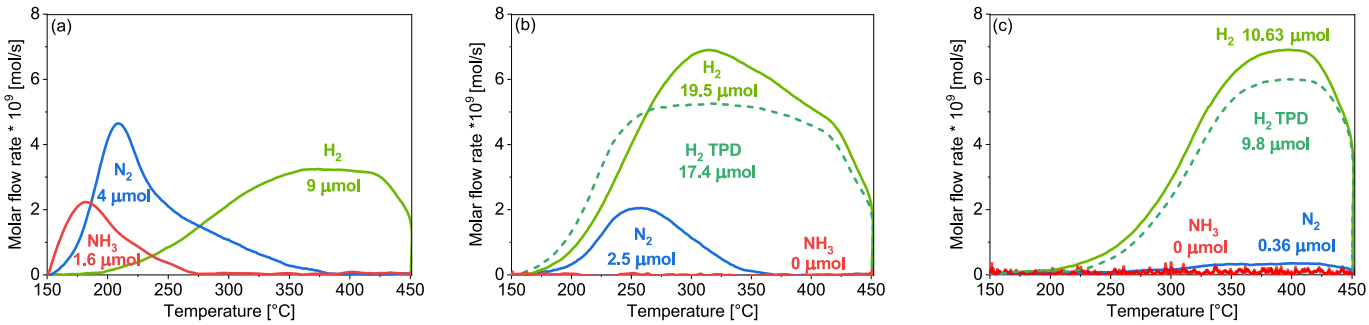

Fig. 13. Ru/CeO_2 1% NH_3-TPD spectra after adsorption at 150 °C (a), 200 °C (b), 300 °C (c).

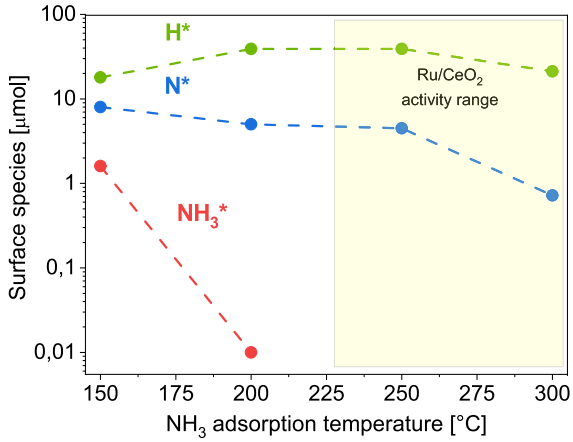

Fig. 14. Estimated surface species after 1% NH_3 adsorption over Ru/CeO_2.

3.5. Mechanistic in situ DRIFTS experiments

In situ DRIFTS experiments were carried out to obtain additional information into the reaction mechanism. Before the measurements, both catalysts were reduced at 450 °C and then cooled under He flow. Samples were then exposed to NH_3 (2.5%)/He and heated from room temperature up to 450 °C. The same procedure was applied to Al_2O_3 and CeO_2 supports for comparison.

Fig. 15 shows the spectra recorded during the temperature ramp under NH_3 atmosphere together with the spectra of the supports under NH_3 atmosphere at room temperature. The spectra acquired during the previous cooling step were used as background. Concerning gaseous or weakly adsorbed NH_3, the typical sharp signals were observed at 1624 cm^{-1}, 930 cm^{-1} and 965 cm^{-1} [32]. On Ru/Al_2O_3, signals at 1270 cm^{-1} and 1625 cm^{-1} can be attributed to NH_3 coordinated to Lewis sites, whereas adsorption on Brønsted acid sites originates peaks at 1450 cm^{-1} and 1690 cm^{-1}. The evident shoulder at 1500 cm^{-1} is reasonably attributed to amide scissoring vibrations while the weak feature at 1385 cm^{-1} is associated to ammonium ions [33–35]. Up to 200 °C no additional signals were visible, with the exception of a band at 1800 cm^{-1}, attributed to isolated ruthenium hydride species [36,37]. The absence of this feature in the spectrum of bare Al_2O_3 confirms that it is strictly related to the presence of ruthenium. Upon heating, the intensity of the signals of the Brønsted sites on Ru/Al_2O_3 decreased progressively, while the signals of the Lewis sites remained visible even at 450 °C. The Ru—H band increased in intensity up to 150 °C, then it rapidly decreased and

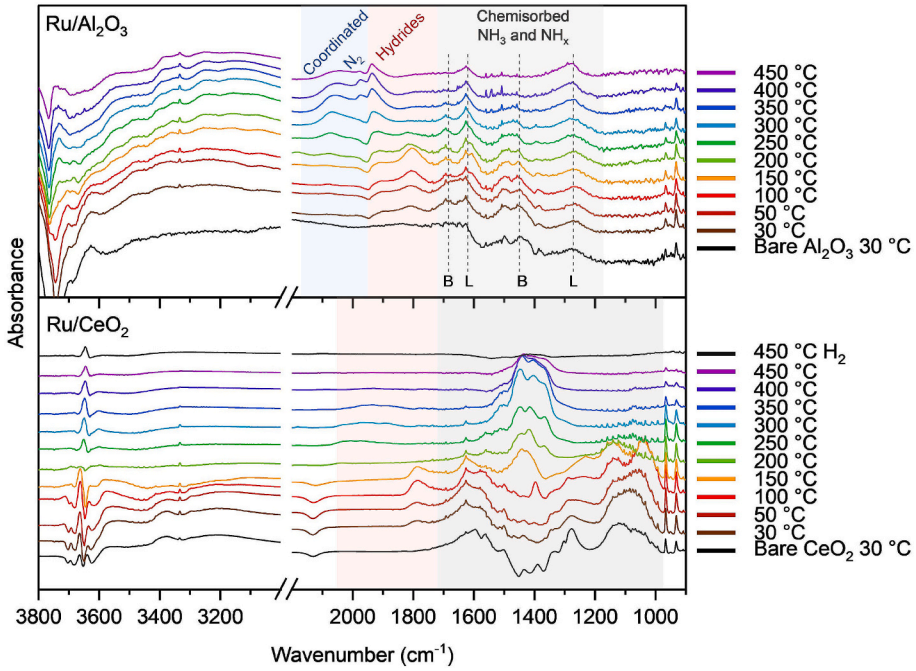

Fig. 15. In situ DRIFTS spectra during NH_3 decomposition over Ru/Al_2O_3 and Ru/CeO_2 catalysts. The black curves at the bottom are the spectra of the supports after reducing pretreatment collected under reaction atmosphere. For Ru/Al_2O_3, dotted lines indicate signals of ammonia adsorbed on Brønsted (B) and Lewis (L) acidic sites. For Ru/CeO_2, the black spectrum at the top was acquired at the end of the pretreatment, under H_2 (5%)/N_2.

fully disappeared at 300 °C, while starting from approximately 250 °C a group of signals appeared in the range 1900–2150 cm^{-1}. The high frequency component of these signals fall in the range of chemisorbed N_2 [38,39], and were therefore assigned accordingly, whereas the peak at 1930 cm^{-1} is more likely related to hydride species [36,37]. In the O—H stretching region of Ru/Al_2O_3, NH_3 adsorption caused a decrease of hydroxyl signals at all temperatures, as evidenced by the negative signal at 3750 cm^{-1}; this feature was accompanied by the formation of a band between 3000 cm^{-1} and 3700 cm^{-1} attributed to N—H stretching of adsorbed NH_3 [40]. Increasing temperature resulted in a general decrease in signal intensity, in line with the lower amount of NH_3 adsorbed onto the support.

In contrast, for Ru/CeO_2 the group of signals in the range 1000–1320 cm^{-1} and the band at 1600 cm^{-1} are attributed exclusively to NH_3 on Lewis sites [35,41–43]. As observed with Ru/Al_2O_3, the weak band at 1800 cm^{-1} is associated to isolated ruthenium hydrides, an assignment corroborated by the absence of this signal in the spectrum of bare CeO_2. The negative signal at 2130 cm^{-1} is indicative of partial reoxidation of the ceria surface, since a peak in this position has been associated to the forbidden electronic transition of Ce^{3+} [44]. Upon heating Ru/CeO_2, the signals associated with chemisorbed ammonia already disappeared at 250 °C, whereas with Ru/Al_2O_3, NH_3 coordinated to Lewis sites remained detectable up to 450 °C, in accordance with the different acidity of the two supports. Ru—H signal on Ru/CeO_2 again increased up to 150 °C but, unlike the alumina case, disappeared completely at 200 °C. At the same temperature, the negative signal at 2130 cm^{-1} disappeared, indicating reduction of surface Ce(IV) back to Ce(III). Increasing further the temperature, new bands appeared: the group of signals in the range 1350–1450 cm^{-1} are attributed to -NH species, produced by further dehydrogenation of ammonia [43,45], likely acting as spectator species accumulated on the ceria surface, while a weak band between 1800 cm^{-1} and 2100 cm^{-1} was tentatively assigned to ruthenium hydrides. In the O—H stretching region of Ru/CeO_2, at temperatures lower than 200 °C the signals between 3600 cm^{-1} and 3750 cm^{-1} are most likely related to rearrangement of hydroxyl groups, while the broad band between 3000 cm^{-1} and 3600 cm^{-1} is composed by N—H stretchings of adsorbed ammonia [46], similarly to Ru/Al_2O_3. However, already at 200 °C these signals disappeared, indicating restoration of hydroxyl groups and removal of adsorbed NH_3. At higher temperatures, a sharp OH vibration appeared at 3650 cm^{-1} together with a weaker feature at 3350 cm^{-1}; the similarity with the spectrum of the catalyst under H_2 atmosphere confirms that surface of ceria is in a reduced state above 200 °C under reaction conditions, in agreement with the behaviour of the band at 2130 cm^{-1}.

A direct comparison of the two catalysts highlights clear differences in the evolution of hydride-related signals. The disappearance of the signal at 1800 cm^{-1} occurred on both catalysts within the temperature range of 150–250 °C, but with an evident anticipation in the case of ceria. At higher temperatures, a new signal attributed to metal hydrides developed on Ru/Al_2O_3, whereas on Ru/CeO_2 a weak hydride signal was present only between 250 °C and 350 °C. Light can be shed on these results by invoking the fundamental studies by Schoss and coworkers on the tendency of Ru nanoparticles to form surface hydrides [19,20]. Their theoretical and experimental results showed that hydrogen easily binds with the surface Ru atoms producing a restructuring of the particles, and that the stoichiometry of the resulting hydride is influenced by their final morphology and size. We can thus infer that the shift of the hydride signals for the alumina-based catalyst is associated to a restructuring of the supported Ru nanoparticles under reactive conditions due to the hydrogen atmosphere. Conversely, the observed capacity of ceria to hinder the formation of Ru-hydrides can be explained considering its ability to displace and store hydrogen. Thus, while NH_3 decomposition on Ru/Al_2O_3 would lead to accumulation of H* on Ru sites and formation of chemical bonds, on Ru/CeO_2 there is a limited coverage of ruthenium by H* species which are consumed at lower temperatures, as becomes evident by integration of hydride signals against temperature (fig. S15). A plausible explanation is that hydrides formed on the metal would be readily transferred to the support. Such transfer, clearly demonstrated by the isotopic switch experiments presented above, is known to be facilitated by the reducibility of cerium dioxide and may involve reduction of Ce(IV) to Ce(III) accompanied by formation of a hydroxyl group, reduction of Ce(IV) to Ce(III) and formation of water and transient cerium hydride species [47,48]. Due to their transient nature and the facile hydrogen mobility on Ru/CeO_2, these species are unlikely to produce a distinct infrared fingerprint.

DRIFTS analysis was also repeated by exposing the catalyst to NH_3 at room temperature only, and desorbing NH_3 under He atmosphere while acquiring the spectra. For brevity, the corresponding results are reported in the Supplementary Information (Fig. S14). The spectra show trends comparable to those observed in Fig. 14, with more pronounced features associated with Ru hydride species and their reactivity.

Summarising, DRIFTS results indicate that at low temperatures both catalysts are covered by NH_3 adsorbed on acidic sites of the supports. Upon heating, NH_3 coverage on Al_2O_3 decreases gradually, with Lewis acid sites still partially occupied at 450 °C, whereas on CeO_2 the surface becomes free of NH_3 already at 200 °C This difference reflects the different acidity of the supports and likely also the earlier onset of activity on Ru/CeO_2 at this temperature. An additional indication of Ru/CeO_2 being reactive already at 200 °C is provided by the disappearance of hydride signal at 1800 cm^{-1}, the evident transformation of the OH region, and the disappearance of negative peak at 2130 cm^{-1}. These observations suggest simultaneous reduction of the support and rearrangement of Ru nanoparticles at this temperature. Above 200 °C, hydride transformation and formation of chemisorbed N_2 are clearly observed on Ru/Al_2O_3, in accordance with catalytic tests indicating NH_3 activation at these temperatures. Notably, a hydride signal remains detectable on Ru/Al_2O_3 at all, temperatures, whereas no hydride is recognized on Ru/CeO_2 above 400 °C. These findings support the hypothesis that the superior activity of Ru/CeO_2 is due to its capacity to store and shuttle hydrogen, thereby limiting its poisoning effect, as emerged from H_2-TPD and isotopic exchange experiments.

4. Conclusions

Ru/CeO_2 catalyst showed enhanced catalytic activity and alleviated hydrogen poisoning with respect to benchmark Ru/Al_2O_3 catalyst. Combined kinetic and mechanistic experiments allowed to shed light on the intrinsic nature of H poisoning on Ru particles and on the effect of the support. In the case of Ru/Al_2O_3 catalyst, H* species were found to be chemically bound to Ru sites in the form of hydrides, which can fully explain the strong inhibitory effect exerted on ammonia decomposition. In the case of Ru/CeO_2 catalyst, the ability of ceria to promote H* scavenging from the metal to the support was found to hinder the formation of hydrides under reaction conditions. Besides, the hydrogen storage capacity of Ru/CeO_2 was shown to be significantly higher than that of Ru/Al_2O_3, such that the efficient hydrogen transfer to the support would leave Ru sites clean and available to participate in the reaction.

Interestingly, the markedly higher activity of Ru/CeO_2 enlarged the testing temperature range, revealing a temperature-dependent transition between kinetic regimes. Extensive kinetic data and independent transient experiments suggest that, at high temperature, the rate determining step lies within the NH_3 dehydrogenation pathway, whereas at the lower temperatures the RDS consists of the associative desorption of N*. A combined kinetic model was developed and successfully validated by experiments outside the fitting field, including experiments with NH_3 feed concentrations up to 50%.

The model robustness makes it a highly reliable tool for reactor engineering applications; this result is especially valuable when considering the supporting mechanistic study that provides an original interpretation of the nature of H-poisoning on Ru, and is of inspiration and relevance for the development of improved catalyst formulations.

CRediT authorship contribution statement

Ivan Conti: Writing – original draft, Validation, Methodology, Investigation, Formal analysis, Data curation. **Daniele Quattrin:** Writing – original draft, Methodology, Investigation, Formal analysis, Data curation. **Yi Qiu:** Writing – original draft, Resources, Methodology, Data curation, Conceptualization. **Alessandro Trovarelli:** Writing – review & editing, Visualization, Validation, Resources, Methodology, Funding acquisition, Formal analysis, Conceptualization. **Alessandra Beretta:** Writing – review & editing, Supervision, Resources, Project administration, Methodology, Formal analysis, Data curation, Conceptualization.

Declaration of competing interest

The authors declare that they have no known competing financial interests or personal relationships that could have appeared to influence the work reported in this paper.

Acknowledgements

This work is supported by the European Union – Next Generation EU, Mission 4 Component 1 CUP G53D23001200006.

Appendix A. Supplementary data

Supplementary data to this article can be found online at https://doi.org/10.1016/j.cej.2026.180111.

Data availability

Data will be made available on request.

References

[1] R. York, S.E. Bell, Energy transitions or additions? Energy Res. Soc. Sci. 51 (2019) 40–43, https://doi.org/10.1016/j.erss.2019.01.008.
[2] D. Weisser, A guide to life-cycle greenhouse gas (GHG) emissions from electric supply technologies, Energy 32 (2007) 1543–1559, https://doi.org/10.1016/j.energy.2007.01.008.
[3] M.M. Aba, I.L. Sauer, N.B. Amado, Comparative review of hydrogen and electricity as energy carriers for the energy transition, Int. J. Hydrog. Energy 57 (2024) 660–678, https://doi.org/10.1016/j.ijhydene.2024.01.034.
[4] K.T. Møller, T.R. Jensen, E. Akiba, H. Li, Hydrogen - a sustainable energy carrier, Prog. Nat. Sci. Mater. Int. 27 (2017) 34–40, https://doi.org/10.1016/j.pnsc.2016.12.014.
[5] I. Lucentini, X. Garcia, X. Vendrell, J. Llorca, Review of the decomposition of Ammonia to generate hydrogen, Ind. Eng. Chem. Res. 60 (2021) 18560–18611, https://doi.org/10.1021/acs.iecr.1c00843.
[6] E. Spatolisano, L.A. Pellegrini, A.R. De Angelis, S. Cattaneo, E. Roccaro, Ammonia as a carbon-free energy carrier: NH_3 cracking to H_2, Ind. Eng. Chem. Res. 62 (2023) 10813–10827, https://doi.org/10.1021/acs.iecr.3c01419.
[7] U. Remme, Global Hydrogen Review 2025, 2025.
[8] A. Hellman, E.J. Baerends, M. Biczysko, T. Bligaard, C.H. Christensen, D.C. Clary, et al., Predicting catalysis: understanding Ammonia synthesis from first-principles calculations, J. Phys. Chem. B 110 (2006) 17719–17735, https://doi.org/10.1021/jp056982h.
[9] J.C. Ganley, F.S. Thomas, E.G. Seebauer, R.I. Masel, A priori catalytic activity correlations: the difficult case of hydrogen production from Ammonia, Catal. Lett. 96 (2004) 117–122, https://doi.org/10.1023/B:CATL.0000030108.50691.d4.
[10] W. Tsai, W.H. Weinberg, Steady-state decomposition of ammonia on the ruthenium (001) surface, J. Phys. Chem. 91 (1987) 5302–5307, https://doi.org/10.1021/j100304a034.
[11] M.C.J. Bradford, P.E. Fanning, M.A. Vannice, Kinetics of NH3Decomposition over well dispersed Ru, J. Catal. 172 (1997) 479–484, https://doi.org/10.1006/jcat.1997.1877.
[12] S. Zhou, S. Lin, H. Guo, First-principles insights into Ammonia decomposition catalyzed by Ru clusters anchored on carbon nanotubes: size dependence and interfacial effects, J. Phys. Chem. C 122 (2018) 9091–9100, https://doi.org/10.1021/acs.jpcc.8b01965.
[13] Y. Qiu, F.S. Franchi, N. Usberti, A. Beretta, Kinetic investigation of NH3 decomposition over Ru-based catalysts: the limiting role of H* surface coverage and its impact on reactor engineering, Fuel Process. Technol. 276 (2025) 108270, https://doi.org/10.1016/j.fuproc.2025.108270.
[14] S.F. Yin, B.Q. Xu, X.P. Zhou, C.T. Au, A mini-review on ammonia decomposition catalysts for on-site generation of hydrogen for fuel cell applications, Appl. Catal. A Gen. 277 (2004) 1–9, https://doi.org/10.1016/j.apcata.2004.09.020.
[15] Y. Qiu, I. Conti, E. Berretti, A. Beretta, Unprecedented promotion of NH_3 decomposition over Ru *via* H_2 -scavenging: a chemical reaction engineering analysis, React. Chem. Eng. (2026) 10.1039.D6RE00086J, https://doi.org/10.1039/D6RE00086J.
[16] Y. Ju, S.W. Byun, Y. Song, B. Kim, K.Y. Kang, H. Kim, et al., Modulated electronic environment of Ru on CeO2 for superior NH3 decomposition catalysis, Sep. Purif. Technol. 374 (2025) 133723, https://doi.org/10.1016/j.seppur.2025.133723.
[17] L.-Y. Yan, X.-P. Fu, W.-W. Wang, C.-J. Jia, Atmosphere-induced Ru-Ov-CeO2 interface for alleviating hydrogen inhibitory effect toward ammonia decomposition, Appl. Catal. B Environ. Energy 378 (2025) 125538, https://doi.org/10.1016/j.apcatb.2025.125538.
[18] X.-C. Hu, X.-P. Fu, W.-W. Wang, X. Wang, K. Wu, R. Si, et al., Ceria-supported ruthenium clusters transforming from isolated single atoms for hydrogen production via decomposition of ammonia, Appl. Catal. B Environ. Energy 268 (2020) 118424, https://doi.org/10.1016/j.apcatb.2019.118424.
[19] D. Bumüller, A.-S. Hehn, E. Waldt, R. Ahlrichs, M.M. Kappes, D. Schooss, Ruthenium cluster structure change induced by hydrogen adsorption: Ru_{19}^-, J. Phys. Chem. C 121 (2017) 10645–10652, https://doi.org/10.1021/acs.jpcc.6b09521.
[20] A.-S. Hehn, D. Bumüller, W. Klopper, M.M. Kappes, D. Schooss, Structural phase transition of ruthenium cluster hydrides, J. Phys. Chem. C 124 (2020) 14306–14315, https://doi.org/10.1021/acs.jpcc.0c01962.
[21] C. Wang, Z. Li, J. Qiu, X. Sun, Y. Ma, C. Wang, et al., Synthesis of efficient Pt/Al2O3 catalyst for the simultaneous removal of NH3 and CO: revealing the rate-determining factor, Appl. Catal. B Environ. Energy 374 (2025) 125367, https://doi.org/10.1016/j.apcatb.2025.125367.
[22] A. Felli, M. Danielis, A. Trovarelli, S. Colussi, Parametric study on Ru/CeO2 ammonia decomposition catalysts for hydrogen production, ChemCatChem 17 (2025) e00585, https://doi.org/10.1002/cctc.202500585.
[23] D. Mears, Diagnostic criteria for heat transport limitations in fixed bed reactors, J. Catal. 20 (1971) 127–131, https://doi.org/10.1016/0021-9517(71)90073-X.
[24] W.J. Movick, F. Kishimoto, K. Takanabe, Dynamic surface-coverage alteration based on microkinetic analysis for enhanced ammonia synthesis over ruthenium catalysts at low temperatures, Chem. Eng. J. 452 (2023) 139525, https://doi.org/10.1016/j.cej.2022.139525.
[25] L.J. Gillespie, J.A. Beattie, The thermodynamic treatment of chemical equilibria in systems composed of real gases. I. An approximate equation for the mass action function applied to the existing data on the Haber equilibrium, Phys. Rev. 36 (1930) 743–753, https://doi.org/10.1103/PhysRev.36.743.
[26] F. Giordano, A. Trovarelli, C. De Leitenburg, M. Giona, A model for the temperature-programmed reduction of low and high surface area ceria, J. Catal. 193 (2000) 273–282, https://doi.org/10.1006/jcat.2000.2900.
[27] J.B. Peri, R.B. Hannan, Surface hydroxyl groups on γ-ALUMINA[1], J. Phys. Chem. 64 (1960) 1526–1530, https://doi.org/10.1021/j100839a044.
[28] B. Lin, R. Wang, X. Yu, J. Lin, F. Xie, K. Wei, Physicochemical characterization and H2-TPD study of alumina supported ruthenium catalysts, Catal. Lett. 124 (2008) 178–184, https://doi.org/10.1007/s10562-008-9483-8.
[29] K. Nakamoto, Applications in Inorganic Chemistry, in: Infrared Raman Spectra Inorg. Coord. Compd., John Wiley & Sons, Ltd, 2008, pp. 149–354, https://doi.org/10.1002/9780470405840.ch2.
[30] G.N. Vayssilov, M. Mihaylov, Pst Petkov, K.I. Hadjiivanov, K.M. Neyman, Reassignment of the vibrational spectra of carbonates, formates, and related surface species on ceria: a combined density functional and infrared spectroscopy investigation, J. Phys. Chem. C 115 (2011) 23435–23454, https://doi.org/10.1021/jp208050a.
[31] J. Pérez-Ramírez, The six-flow reactor technology a review on fast catalyst screening and kinetic studies, Catal. Today 60 (2000) 93–109, https://doi.org/10.1016/S0920-5861(00)00321-7.
[32] G. Herzberg, Molecular Spectra and Molecular Structure: Volume II: Infrared and Raman Spectra of Polyatomic Molecules, Van Nostrand-Reinhold, 1950.
[33] F. Kapteijn, L. Singoredjo, M. Vandriel, A. Andreini, J.A. Moulijn, G. Ramis, et al., Alumina-supported manganese oxide catalysts: II. Surface characterization and adsorption of ammonia and nitric oxide, J. Catal. 150 (1994) 105–116, https://doi.org/10.1006/jcat.1994.1326.
[34] M. Amblard, R. Burch, B.W.L. Southward, A study of the mechanism of selective conversion of ammonia to nitrogen on Ni/γ-Al2O3 under strongly oxidising conditions, Catal. Today 59 (2000) 365–371, https://doi.org/10.1016/S0920-5861(00)00301-1.
[35] A.A. Tsyganenko, D.V. Pozdnyakov, V.N. Filimonov, Infrared study of surface species arising from ammonia adsorption on oxide surfaces, J. Mol. Struct. 29 (1975) 299–318, https://doi.org/10.1016/0022-2860(75)85038-1.
[36] Y. Izumi, K. Aika, Promoted catalysis by supported [Ru6N] clusters in N2 and/or H2: structural and chemical controls, J. Phys. Chem. 99 (1995) 10346–10353, https://doi.org/10.1021/j100025a042.
[37] X. Wang, L. Andrews, Infrared spectra and theoretical calculations for Fe, Ru, and Os metal hydrides and dihydrogen complexes, J. Phys. Chem. A 113 (2009) 551–563, https://doi.org/10.1021/jp806845h.
[38] K. Ogasawara, M. Miyazaki, K. Miyashita, H. Abe, Y. Niwa, M. Sasase, et al., Ammonia decomposition over water-durable hexagonal $BaTiO_{3-x}N_y$-supported Ni catalysts, Adv. Energy Mater. 13 (2023) 2301286, https://doi.org/10.1002/aenm.202301286.

[39] K. Nakamoto, Applications in Coordination Chemistry, in: Infrared Raman Spectra Inorg. Coord. Compd., John Wiley & Sons, Ltd, 2008, pp. 1–273, https://doi.org/10.1002/9780470405888.ch1.
[40] L. Zhang, H. He, Mechanism of selective catalytic oxidation of ammonia to nitrogen over ag/Al2O3, J. Catal. 268 (2009) 18–25, https://doi.org/10.1016/j.jcat.2009.08.011.
[41] G. Ramis, L. Yi, G. Busca, Ammonia activation over catalysts for the selective catalytic reduction of NOx and the selective catalytic oxidation of NH3. An FT-IR study, Catal. Today 28 (1996) 373–380, https://doi.org/10.1016/S0920-5861(96)00050-8.
[42] G. Qi, R.T. Yang, R. Chang, MnO_x-CeO_2 mixed oxides prepared by co-precipitation for selective catalytic reduction of NO with NH_3 at low temperatures, Appl. Catal. B Environ. 51 (2004) 93–106, https://doi.org/10.1016/j.apcatb.2004.01.023.
[43] Y. Guo, L. Ma, Z. Li, Z. Liu, H. Chang, X. Zhao, et al., Specific reactivity of 4d and 5d transition metals supported over CeO2 for ammonia oxidation, Cat. Sci. Technol. 12 (2022) 6507–6517, https://doi.org/10.1039/D2CY01380K.
[44] C. Binet, A. Badri, J.-C. Lavalley, A spectroscopic characterization of the reduction of ceria from electronic transitions of intrinsic point defects, J. Phys. Chem. 98 (1994) 6392–6398, https://doi.org/10.1021/j100076a025.
[45] H. Liu, R. Zhang, S. Liu, G. Liu, CeO2/Ni inverse catalyst as a highly active and stable Ru-free catalyst for Ammonia decomposition, ACS Catal. 14 (2024) 9927–9939, https://doi.org/10.1021/acscatal.4c02313.
[46] Z. Ma, D. Weng, X. Wu, Z. Si, Effects of WO*x* modification on the activity, adsorption and redox properties of CeO2 catalyst for NO*x* reduction with ammonia, J. Environ. Sci. 24 (2012) 1305–1316, https://doi.org/10.1016/S1001-0742(11)60925-X.
[47] C. Copéret, D.P. Estes, K. Larmier, K. Searles, Isolated surface hydrides: formation, structure, and reactivity, Chem. Rev. 116 (2016) 8463–8505, https://doi.org/10.1021/acs.chemrev.6b00082.
[48] Z. Wu, Y. Cheng, F. Tao, L. Daemen, G.S. Foo, L. Nguyen, et al., Direct neutron spectroscopy observation of cerium hydride species on a cerium oxide catalyst, J. Am. Chem. Soc. 139 (2017) 9721–9727, https://doi.org/10.1021/jacs.7b05492.